doi link: https://doi.org/10.1016/j.combustflame.2021.111692

On the Radical Behavior of Large Polycyclic Aromatic Hydrocarbons in Soot Formation and Oxidation

Andrea Nobili[a], Luna Pratali Maffei[a], Alberto Baggioli[b], Matteo Pelucchi[a], Alberto Cuoci[a], Carlo Cavallotti*[b], Tiziano Faravelli[a]

[a]*Department of Chemistry, Materials and Chemical Engineering "G. Natta", Politecnico di Milano, P.zza Leonardo da Vinci 32, 20133, Milano, Italy*
[b]*Department of Chemistry, Materials and Chemical Engineering "G. Natta", Politecnico di Milano, P.zza Leonardo da Vinci 32, 20133, Milano, Italy*

*Corresponding author

E-mail address: carlo.cavallotti@polimi.it

Abstract

The mechanism of evolution of polycyclic aromatic hydrocarbons (PAHs) into carbonaceous particles in combustion, atmosphere, and interstellar space has been the subject of intense debate. Recently, there has been emerging evidence supporting resonantly-stabilized radicals as key players in PAH growth. In this work, we build on this hypothesis and propose that, beyond a critical size, PAH reactivity can be assimilated to that of radicals. We found that odd-C-numbered PAHs embedding 5-membered rings rapidly lose a hydrogen atom to form resonantly-stabilized radicals in combustion conditions, while even-C-numbered PAHs react as open-shell rather than closed-shell molecules independently of temperature, as usually assumed. Acenes were used as molecular models of large even-C-numbered PAHs. The construction of a kinetic model including these findings allows to interpret experimental soot oxidation data otherwise irreconcilable with existing chemical kinetic mechanisms.

***Keywords*:** Kinetic Model, Soot growth mechanism, PAH, π-radicals, open-shell diradicals

1. Introduction

Carbonaceous particles generated in combustion (i.e. soot), in the atmosphere, and in interstellar space are a continuous source of scientific attention and debate. Their negative impact on everyday life is well known. Health diseases like cancer [1] and climate change [2] are the most evident phenomena, triggering public awareness and motivating research efforts towards the mitigation of their harmful effects. New evidence has recently related soot particles to the COVID-19 pandemic, because of their possible interactions with respiratory droplets [3, 4]. On the other hand, in-flame synthesis of carbon nanoparticles with specific optical and electronic properties is becoming, technically and economically, a viable route to produce novel high-performance materials for sensors and catalysis [5].

Despite the wide interest, soot formation pathways are far from being fully understood [6, 7]. In particular, conclusive evidence about the phenomena controlling the transition from gas-phase to incipient soot is still missing [8], though the role of polycyclic aromatic hydrocarbons (PAHs) as soot precursors finds a major consensus within the scientific community [6, 9]. On this note, a recent paper [7] highlighted the importance of resonance-stabilized radicals (RSRs) in soot inception and growth. The authors proposed a mechanism called CHRCR (clustering of hydrocarbons by radical chain reactions), which describes the PAH growth through reactions between RSR and other hydrocarbons. These reactions, while leading to the growth of heavier PAHs, allow the regeneration of RSRs. Other experimental evidence [10,11] suggests that stable and persistent radicals are abundant in large PAHs and incipient soot. Consequently, an open question arises about the actual chemical nature of soot particles, which are commonly modeled as entities requiring surface activation (through H-abstraction) in order to grow and oxidize [12, 13].

This work provides an answer through the investigation of the prevailing electronic structure and associated reactivity of PAHs in combustion environments. The paper is organized as follows. The adopted computational methodology is described in section 2, while the computational predictions on the reactivity of odd and even PAHs are reported in section 3.1 and 3.2. The impact of the findings reported in sections 3.1 and 3.2 is finally evaluated in section 3.3 by means of kinetic simulations with a soot model built starting from its previous version [9] upon the theoretical results obtained in this

work. Though a detailed description of the updated soot model along with its extensive validation lies outside the main objective of this work and will be presented in upcoming papers, some representative examples of the model performances are shown to highlight the improved predictive capabilities, especially for soot oxidation in reacting environments lacking of particle activating species.

2. Methodology

2.1. Computational approach

Energies and thermodynamic properties of all the investigated chemicals species were determined from first principles using the Rigid Rotor Harmonic Oscillator approximation (RRHO). Most ab initio electronic structure calculations were performed using density functional theory (DFT) using Gaussian09 [14] with the M06-2X [15] functional and the 6-311+G(d,p) basis set [16]. The M06-2X functional was selected as it is suitable to describe chemical kinetics at a reasonable level of accuracy, predicts singlet-triplet energy gaps (ΔE_{S-T}) for acenes in remarkable agreement with experimental data and [17], and accounts reasonably well for noncovalent interactions, of particular relevance in aromatic systems [18]. It is also noteworthy that the M06-2X has been used with success to study acene dimerization [19], a reactive system similar to those here investigated. A benchmark of the chosen computational methodology is provided in section S3 of the Supplementary Material.

Several of the reactions investigated in the present study have reactants with a significant singlet diradical character. In those cases, calculations were performed using unrestricted wavefunctions and broken symmetry guesses, as it was shown that this methodology, computationally much cheaper than the theoretically more proper multireference methods, gives a reasonable description of these systems [19]. Indeed, considering the size of the species involved in this study (up to 46 C-atoms PAHs), the chosen computational methodology approaches the maximum level of accuracy achievable for the investigated systems at a reasonable computational cost.

Frequency calculations were performed for all minimum energy structures and saddle points. Minima were characterized by the absence of imaginary vibrational frequencies, while saddle points have just a single imaginary frequency. All the reported energies were corrected with the calculated ZPE. Rate constants of H-addition on linear

acenes have been computed from master equation (ME) calculations using the MESS solver [20]. Master equation input files were generated with EStokTP [21], designed to automatically couple electronic structure calculations, transition state theory, and ME simulations to produce a priori predictions of temperature and pressure dependent rate constants. Spin population analysis was carried out on Multiwfn [22] using Becke atomic spaces [23]. MECP structures were determined using triplet minimum energy structures as guess at the M06-2X/6-311+g(d,p) level, while spin-orbit coupling factors were calculated using CASSCF wavefunctions with a Breit-Pauli Hamiltonian, as implemented in Molpro [24].

2.2 Flame simulations

Numerical simulations of laminar premixed fuel-rich flames were carried out within the OpenSMOKE++ framework [25], using the 1-D laminar flame solver, including the mixture-averaged diffusion model, the Soret effect, and particle thermophoresis in species transport equations. Temperature profiles were imposed from the measurements provided in the literature for each specific flame to account for conductive and radiative heat losses. The computational grid was automatically refined through the analysis of solution gradient and curvature to ensure the smoothness of the calculated profiles. The premixed laminar flames here simulated along with their operating conditions are summarized in Table 1.

Table 1. Set of tested premixed laminar flames. Six premixed laminar flames were simulated to evaluate the maximum H-atom mole fraction at different maximum flame temperatures, as reported in Fig. 1c. The maximum H-atom mole fraction is used to compute the selected PAH radical to molecule mole fraction ratio through Eq. (1).

Flame	Inlet mixture	T_{max} (K)	Φ	P (atm)	Reference
F1	C_2H_4/O2 (v0=2 cm/s)	1522	2.4	1	[26]
F2	$nC_7H_{16}/O_2/N_2$	1614	1.9	1	[27]
F3	C_2H_4/O_2 (v_0=4 cm/s)	1723	2.4	1	[26]
F4	C_2H_6/O_2/Ar	1799	2.0	1	[28]
F5	C_4H_6/O_2/Ar	2050	2.4	0.03	[29]
F6	C_6H_6/O_2	2198	2.6	0.03	[10]

2.3 Pseudo equilibrium calculations

Detailed balance, i.e. Eq. (1), is applied to compute odd-C-numbered PAH molecules and π-radicals mole fraction ratio at the assigned operative conditions from the equilibrium reaction PAH↔H+πPAH, where the forward reaction describes the C-H bond dissociation of the methylene group in an odd-C-numbered PAH to a resonantly stabilized radical. The reason why detailed balance is adequate to determine the mole fraction of π-PAH ($x_{\pi PAH}$) is that the characteristic time for the forward and backward processes at typical combustion temperatures are much smaller than the residence time in flames.

$$\frac{x_{\pi PAH}}{x_{PAH}} = exp\left(-\frac{\Delta G_r^0(T, P_{ref})}{RT}\right)\frac{1}{x_{\mathrm{H}}}\frac{P_{ref}}{P} \quad (1)$$

The change in the Gibbs free energy (ΔG_r^0) as a function of temperature is computed from the enthalpy (ΔH_r^0) and entropy (ΔS_r^0) of reaction through Eq. (2), while the H-atom mole fraction is evaluated at the maximum temperature of each premixed laminar flame reported in Table 1:

$$\Delta G_r^0 = \Delta H_r^0 - T\Delta S_r^0 \quad (2)$$

ΔH_r^0 is computed as the energy difference between products and reactants at temperature T, while ΔS_r^0 is computed through statistical thermodynamics.

2.4 Detailed soot kinetic model

The CRECK soot model is coupled to the in-house extensively validated gas-phase kinetic mechanism [9, 30] to follow the transition from gas-phase combustion to solid particles. It discretizes heavy PAHs and soot particles into 25 sections of lumped pseudo species, called BINs, containing from 20 to over 10^8 C-atoms, with a spacing factor of 2 [9], as shown in Table 2. Each section consists of three subsections of different H/C ratio. Molecules and reactive radicals are distinguished up to structures with 80 C-atoms, i.e. BIN1-3, while the largest gas-phase PAH, i.e. BIN4, and the entirety of soot particles and aggregates with more than 100 C-atoms behave as stable radicals only, with delocalized electrons, according to the theoretical results presented in this work. BIN5 is selected as the smallest soot particle, with a diameter D_p ~2 nm. Soot particles, i.e. BIN5-12, are assumed spherical, while BIN13-25 are considered as aggregates with a fractal

dimension of 1.8. BIN12, with $4 \cdot 10^4$ C-atoms and D_p ~10 nm, represents the primary particles and constitutes the building block of fractal aggregates. Each aggregate is composed by a different number of primary particles (Np) according to its total number of C-atoms. Particle and aggregate densities are equal to 1.5 g/cm^3. The thermochemical and diffusion properties of soot pseudo-species are computed through the widely accepted group additivity method and aerosol dynamics theory as described elsewhere [9]. Different reaction classes are implemented to rigorously describe the main chemical and physical pathways of soot, as summarized in Table 3. They include soot inception, growth, coagulation, dehydrogenation, and oxidation processes, whose kinetics is updated from the previous version of the soot model [9] to account for the peculiar radical reactivity of large aromatic structures discussed in this work.

Table 2. Properties of lumped pseudo-species, i.e. BINs.

BIN	C-atoms	Mass [amu]	D_p [nm]	H/C ratio		
				A	B	C
		Heavy PAHs				
BIN1	20	250	0.81	0.8	0.5	0.2
BIN2	40	500	1.02	0.775	0.4	0.2
BIN3	80	1000	1.28	0.75	0.3	0.1
BIN4	160	2000	1.60	0.725	0.2	0.05
		Soot Particles				
BIN5	320	$4 \cdot 10^3$	2.02	0.7	0.2	0.05
BIN6	640	$8 \cdot 10^3$	2.55	0.675	0.2	0.05
BIN7	$1.25 \cdot 10^3$	$1.55 \cdot 10^4$	3.18	0.65	0.2	0.05
BIN8	$2.5 \cdot 10^3$	$3 \cdot 10^4$	4.01	0.625	0.2	0.05
BIN9	$5 \cdot 10^3$	$6 \cdot 10^4$	5.05	0.6	0.2	0.05
BIN10	$1 \cdot 10^4$	$1.2 \cdot 10^5$	6.37	0.575	0.2	0.05
BIN11	$2 \cdot 10^4$	$2.45 \cdot 10^5$	8.02	0.55	0.2	0.05
BIN12	$4 \cdot 10^4$	$4.9 \cdot 10^5$	10.11	0.525	0.2	0.05
		Soot Aggregates				
BIN13	$8 \cdot 10^4$	$9.7 \cdot 10^5$	12.73	0.5	0.2	0.05
BIN14	$1.6 \cdot 10^5$	$1.95 \cdot 10^6$	16.04	0.475	0.2	0.05
BIN15	$3.2 \cdot 10^5$	$3.9 \cdot 10^6$	20.21	0.45	0.2	0.05
BIN16	$6.4 \cdot 10^5$	$7.8 \cdot 10^6$	25.47	0.425	0.2	0.05
BIN17	$1.25 \cdot 10^6$	$1.51 \cdot 10^7$	31.83	0.4	0.2	0.05
BIN18	$2.5 \cdot 10^6$	$3.02 \cdot 10^7$	40.11	0.375	0.2	0.05
BIN19	$5 \cdot 10^6$	$6.02 \cdot 10^7$	50.53	0.35	0.2	0.05
BIN20	$1 \cdot 10^7$	$1.21 \cdot 10^8$	63.66	0.325	0.2	0.05
BIN21	$2 \cdot 10^7$	$2.41 \cdot 10^8$	80.21	0.3	0.2	0.05
BIN22	$4 \cdot 10^7$	$4.82 \cdot 10^8$	101.06	0.3	0.2	0.05
BIN23	$8 \cdot 10^7$	$9.64 \cdot 10^8$	127.33	0.3	0.2	0.05
BIN24	$1.6 \cdot 10^8$	$1.93 \cdot 10^9$	160.12	0.3	0.2	0.05
BIN25	$3.2 \cdot 10^8$	$3.86 \cdot 10^9$	202.12	0.3	0.2	0.05

Table 3. Reaction classes in the soot kinetic model. See Dataset S1 for the complete set of kinetic parameters.

Reaction class	Reference
Acetylene addition	this work
Resonant radical addition	[9]
Soot inception	[9]
PAH condensation	this work
Particle coagulation and agglomeration	[9]
Dehydrogenation	[9]
Demethylation	[9]
Surface oxidation	this work
Oxidation-induced fragmentation	[12]

3. Results and discussion

The reactivity of PAHs changes depending on whether the total number of carbon atoms is odd or even [10]. The chemical nature and reactivity of odd and even PAHs was therefore investigated using different approaches in sections 3.1 and 3.2, while the impact of the findings on their kinetics is studied in section 3.3.

3.1 Reactivity of odd-C-numbered species

Though odd-C-numbered PAHs that may form during combustion have a huge variety of possible structures, they are generally characterized, in their nonradical state, by the presence of a methylene group (R_n-CH_2-R_n) within a ring. Their most stable resonance-stabilized π-radicals are formed by the removal of a H atom from the methylene group itself, by H-abstractions or unimolecular bond fission reactions. Such RSRs are similar to those detected in flames by recent groundbreaking efforts [7, 11]. Figure 1a shows some representative PAH radicals here investigated, while other related isomers are reported in Fig. S1 of the Supplementary Material. The selected odd-C-numbered PAHs were subdivided in three groups by systematically adding fused-benzene rings to different edges of indene and phenalene, considered as the simplest precursors. In group I, the methylene bridge is located on the free-edge carbon atom of the partially embedded pentagonal ring (blue symbols). In groups II and III it is located on the saturated carbon atom of the peripheral pentagonal (red symbols) and

benzenoid ring (green symbols), respectively. For each PAH, the relative thermodynamic stability of the molecule and the corresponding π-radical as a function of the molecular size is determined by the C–H bond dissociation energy (BDE) of the methylene group, computed as the PAH→H+πPAH enthalpy of reaction at 0 K (ΔH_r^0), since the entropy change is similar for all investigated reactions. The C–H BDE is almost constant (~80 kcal/mol) within group I, indicating a persistent higher stability of molecules over π-radicals with partially embedded pentagonal rings. Conversely, the C–H BDE decreases by 20–30 kcal/mol from 13 to 25 C-atoms for PAHs in groups II and III, indicating the tendency of such large aromatic π-radicals to become more stable than the parent molecules for increasing molecular weight. The propensity of each investigated species to lose a hydrogen atom forming the corresponding π-radicals can be determined applying detailed balance, provided that atomic H concentration is known. Fig. 1b collects the maximum H molar fraction computed for six representative sooting flames, i.e. F1 through F6 reported in Table 1, in the temperature range of interest for soot formation (T≈1500–2200 K), while the PAH radical-to-molecule mole fraction ratio computed through detailed balance is reported in Fig. 1c. Results show that odd-C-numbered PAHs are predominantly π-radicals for flames with T_{MAX}>1900 K, a condition often reached in sooting flames. In addition, molecules of groups II and III are more stable as π-radicals in the whole temperature range, especially as their size increases. This is determined by the low stability of π-PAH radicals with the unpaired electron localized on the partially embedded pentagonal ring, unlike π-PAH radicals of groups II and III, where the unpaired electron is delocalized along the large aromatic structure (see [33] and Supplementary Material). Notably, most of the latter structures are similar to the predominant RSRs detected in atmospheric premixed and diffusion laminar flames [7]. Although no experimental measurements of the relative concentration of large PAH molecules and radicals of the three groups considered have been reported, it is reasonable to assume that partially embedded pentagonal rings, peripheral pentagonal rings, and benzenoid rings, all coexist in large PAHs, thus providing several methylene groups as sources of both localized and delocalized unpaired electrons. Therefore, in the revision of our kinetic model, we assumed a radical behavior for odd-C-numbered PAH containing from about 300 up to more than 300 million C-atoms.

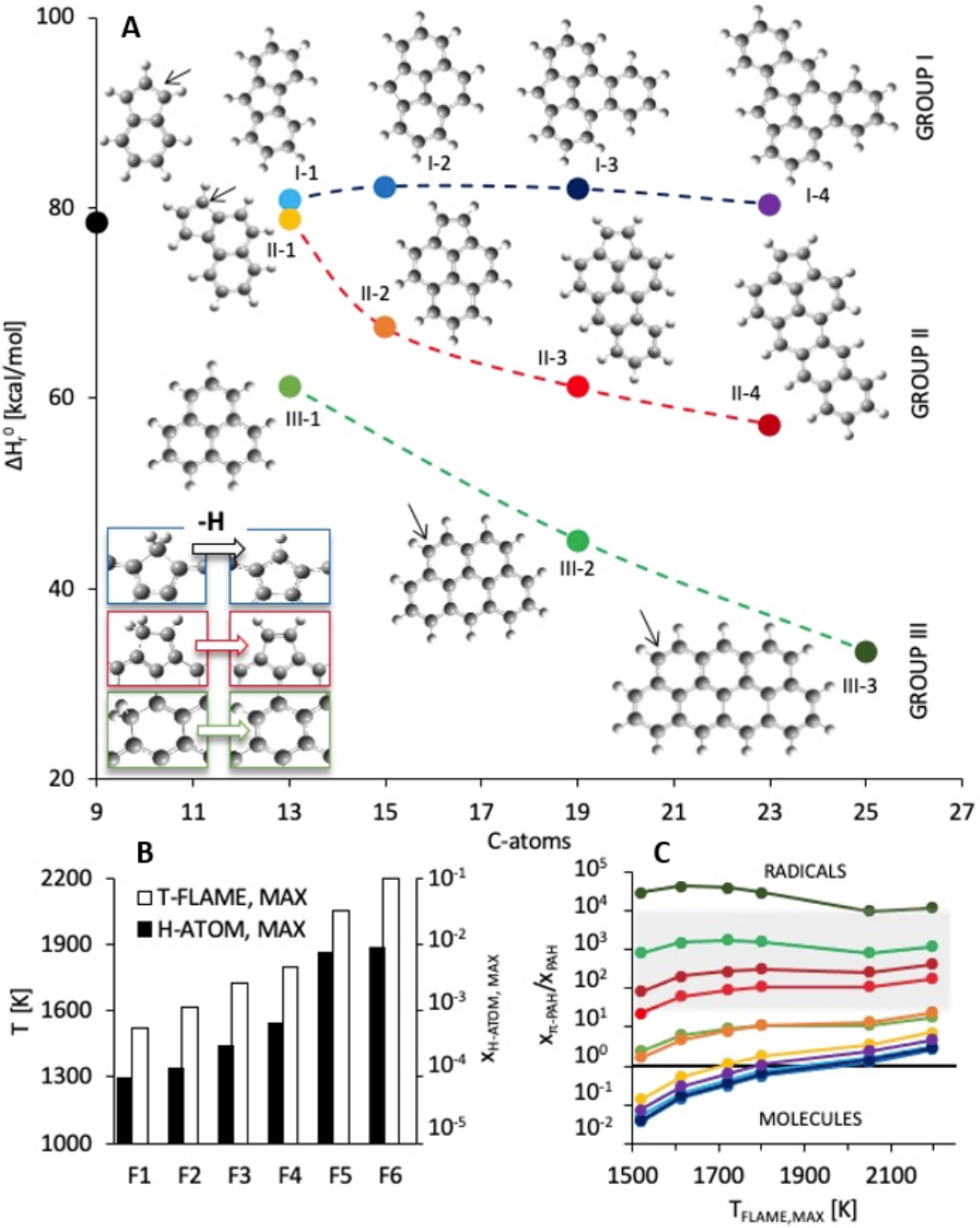

Fig. 1. Relative stability and concentration of odd-C-numbered PAHs and π-radicals in flames. (a) Odd-C-numbered PAH with 2/3 free-C-edge (group II, red symbols) penta-rings and benzenoid rings (group III, green symbols) are characterized by a decrease of the C–H bond energy with the increase of C-atoms number, favoring the formation of π-radicals as sketched in the bottom-left side, unlike PAHs with partially embedded pentagonal rings (group I, blue symbols). Dashed lines are drawn to guide the eye. Black arrows indicate the position of the methylene group in the parent closed-shell structure (the most stable isomer, see also Supplementary Materials). (b) Maximum H mole fraction at different maximum flame temperatures of premixed laminar flames simulations (see Table 1), used to compute (c) the π-radicals-to-molecules mole fraction ratio. The shaded area indicates the region where π-radicals are more abundant than molecules, i.e. PAH radical-to-molecule mole fraction ratio larger than 1. Color codes are the same as in (a).

3.2 Reactivity of even-C-numbered species

For even-C-numbered PAHs we selected molecules composed of several 6-membered aromatic rings as reference, namely acenes and peri-acenes of different sizes, as it is often assumed in literature [6]. In this regard, soot inception is still an open issue, for which different pathways have been proposed over the years [6, 34]. So far, all these mechanisms are based on large PAHs, described either as massive single peri-acenes or as smaller peri-acene islands connected by aliphatic bridges [35]. Experimental evidence of the presence of peri-acenes in nanoparticles formed during combustion was recently reported as obtained via atomic force microscopy. The authors observed “molecules containing fused six-ring units organized in almost entirely peri- 6 condensed structures and several molecules exhibiting aliphatic side-groups” [11]. Due to the chemical similarity between the zigzag edges of acenes and the surface of peri-condensed PAHs and soot particles, which has already been exploited in the study of soot growth [36, 37], peri-acenes represent a convenient model useful to the study of peri-condensed PAHs and soot particles [6]. As it is known [38], the triplet-singlet energy gap (ΔE_{S-T}) in acenes decreases with molecular weight. Here, we computed singlet-triplet energy gaps of linear acenes (Fig. 2), obtaining an excellent agreement (the maximum difference is 1.6 kcal/mol) with experimental data available in literature [17, 39-41] and previous theoretical calculations [38, 42]. To prove whether the decrease of ΔE_{S-T} with molecular size is a common feature of even-C-numbered PAHs, we extended the analysis to PAHs generated from acenes adding fused benzene rings and peri-acenes [m,2], i.e. containing two rows of linear acenes, which mimic more closely the structures of PAHs formed in uncontrolled combustion environments (Fig. 2). They all show a vanishing ΔE_{S-T} with the increase of molecular weight, thus indicating that the triplet state has an energy similar to that of the singlet state.

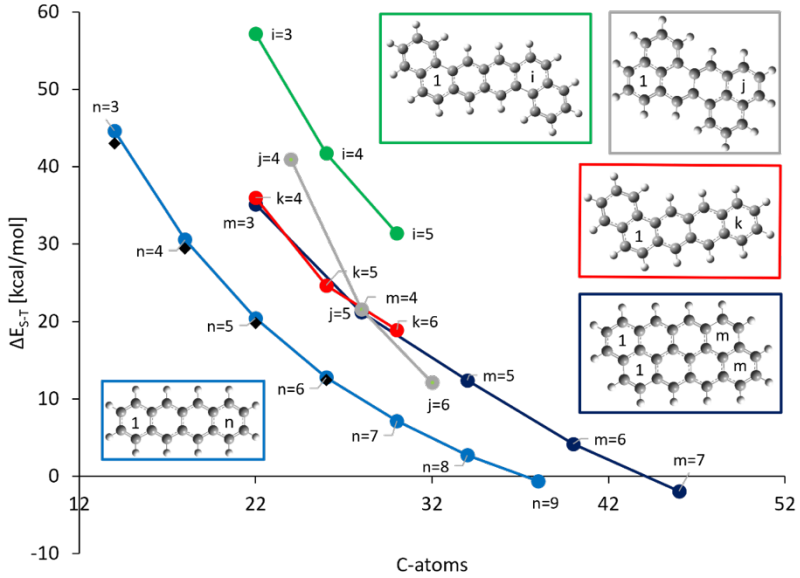

Fig. 2. Singlet-triplet energy gaps ($\Delta E_{S\text{-}T}$) of even-C-numbered PAHs representative of soot. The computed values (circles) of $\Delta E_{S\text{-}T}$ for linear, double, and distorted acenes highlight a systematic trend toward an electronic triplet ground state of large aromatic structures that feature chemical traits similar to those of soot. Black diamonds represent the measured $\Delta E_{S\text{-}T}$ for linear acenes [17, 39-41]. Lines are drawn to guide the eye.

Although the decrease of $\Delta E_{S\text{-}T}$ with molecular weight illustrated for acenes is well known, its impact on molecular reactivity remains to be established. For this reason, we performed hydrogen affinity and rate constant calculations for the addition of H atoms to linear acenes, from pentacene up to octacene (Fig. 3), following the procedures we recently implemented [21]. The most interesting result is that energy barriers for atomic hydrogen addition to the external zigzag site monotonically decrease from 3.9 kcal/mol for pentacene to –0.8 kcal/mol for octacene (Fig. 3a). Moreover, energy barriers become markedly submerged for addition to the inner zigzag sites. The inverse proportionality between barrier height and spin density, describing the localization/delocalization of unpaired electron density, shows that the reactivity of acenes is directly related to a radical-like behavior (Fig. 3b). Further confirmation is obtained by computing the rate constant of H additions on acenes (Fig. 3c). With the increase of the acene molecular weight, this rate constant moves from typical values of H-atom addition reactions on aromatic molecules (rate constant of reaction $H+C_6H_6$ is reported as reference), to those of radical recombination reactions (e.g. $H+C_6H_5$).

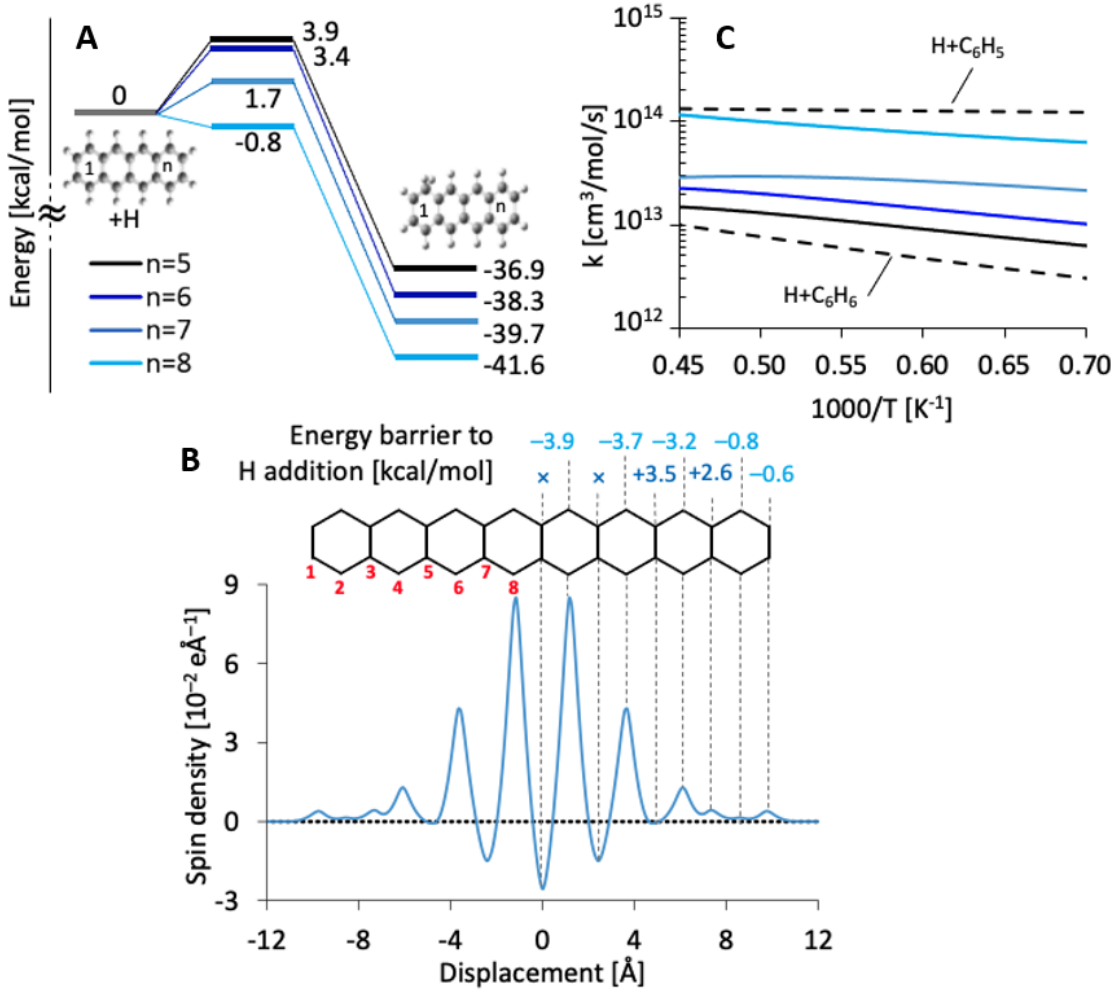

Fig. 3. Radical character of linear acenes toward H addition. (a) Potential energy surface (PES) of H atom addition reactions to the external ring zigzag site in linear acenes. (b) Spin density for octacene, computed as a function of longitudinal displacement from center of mass, reaction site numbering (left) and energy barriers (right) for addition to zigzag sites. The × indicates that the product of the addition reaction is unstable. (c) Per-site high pressure rate constant for H atom addition to acenes computed using conventional transition state theory [21] compared with literature values for $H+C_6H_6$ and $H+C_6H_5$.

With reference to Fig. 3b, the reactivity of hydrogenated zigzag sites increases from peripheral to inner sites in correlation with the trend of calculated spin density. Outer-most and inner-most hydrogenated zigzag sites 2 and 8 were therefore chosen as reference addition positions to quantitatively investigate the capability of octacene to react with a selection of species known to play a key role in soot growth and oxidation: H, CH_3, $O(^3P)$, C_2H_2, and O_2. The corresponding energy barriers are collected in Table 2. We expect these results to be representative of the reactivity of the whole even-C-numbered peri-condensed PAH family, assuming a vanishing singlet-triplet energy gap for large enough

molecular sizes. The results shown in Fig. 2 indicate that peri- and distorted acenes exhibit behaviors similar to those observed for linear acenes. In particular, it should be noted that our intent is to predict the reactivity of PAHs with more than one hundred carbon atoms, hence it appears quite likely that, with the increase of molecular size, different regions with structural features similar to those of octacene will emerge.

Table 4. Energy barriers and energy changes calculated for the addition of several key combustion species to octacene (kcal/mol). Site numbering refers to Fig. 3 and spin multiplicity to that of the full PES, thus inclusive of the two reactants.

		Site 2		Site 8	
Species	Spin Multiplicity	E_{barr}	ΔE (0K)	E_{barr}	ΔE (0K)
H	2	-0.8	-41.7	-3.9	-66.3
CH_3	2	1.5	-31.7	-6.2	-56.8
$O(^3P)$	3	-3.8	-66.4[a]	[b]	-58.3[c]
C_2H_2	3	42.2	31.2	21.9	4.8
O_2	3	24.9	22.6	5.5	-2.6

[a]bridge; [b]barrierless; [c]peroxy.

The energy barriers reported in Table 4 suggest that the interaction of both CH_3 and $O(^3P)$ with octacene is reminiscent of radical species, with $O(^3P)$ addition to site 8 being barrierless. A moderate reactivity is also observed for C_2H_2 and O_2, which can however be significantly enhanced if transition to the singlet PES takes place rapidly. For example, C_2H_2 addition on the singlet PES can take place through concerted and stepwise mechanisms with energy barriers of 14.8 and 28.8 kcal/mol, and is exothermic by -64.2 and 38.0 kcal/mol, respectively.

Because singlet-triplet intersystem crossing (ISC) may enhance considerably even-C-numbered PAHs reactivity, we also investigated in detail the kinetics of this process using nonadiabatic transition state theory (NA-TST) [43] estimating crossing coefficients using Landau Zener theory, as recently implemented in EStokTP [44]. Minimum energy crossing points (MECPs) between triplet and singlet PESs (E_{MECP}) for the investigated acenes are reported in Table 5, together with rate constants determined at different temperatures. To our knowledge this is the first time that ISC rates have been computed for acenes.

Table 5. MECP energies and ISC rates computed using NA-TST for several acenes.

Species	ΔE_{S-T} (kcal/mol)	E_{MECP} (kcal/mol)	SO (cm^{-1})	CLZ[a] ($cm^{-0.5}$)	k(300K) (s^{-1})	k(1000K) (s^{-1})	k(1500K) (s^{-1})	k(2000K) (s^{-1})
naphtalene	64.8	85.4	0.13	1.5E-5	5.7E-55	2.4E-11	3.7E-05	4.4E-02
antracene	44.6	69.1	0.14	2.8E-5	2.2E-43	3.7E-08	3.6E-03	9.8E-01
tetracene	30.6	61.1	0.14	3.4E-5	1.6E-37	2.3E-06	5.8E-02	5.3E+00
pentacene	20.4	52.6	0.14	4.3E-5	1.7E-31	9.0E-05	5.1E-01	1.1E+01
hexacene	12.8	47.6	0.14	3.1E-5	5.9E-28	8.8E-04	1.9E+00	1.2E+01
heptacene	7.1	43.8	0.14	3.0E-5	5.4E-25	8.9E-03	6.8E+00	1.9E+01
octacene	2.7	1.1	0.01	5.4E-9	1.4E+03	6.8E+03	8.1E+03	8.2E+03

[a]CLZ is the ratio between the square of the SO coupling coefficient and the difference of the gradients on the triplet and singlet PESs, as defined in [44].

The NA-TST crossing rates reported in Table 5 highlight a significant dependence on molecular size, which is related to the degree of deformation the acene undergoes at the MECP. For acenes consisting of two up to seven units, the MECP is characterized by a significant distortion, with a tilt of the CH zigzag group out of the molecular plane by about 30-40 degrees. As ΔE_{S-T} decreases, smaller in-plane deformations are required to reach the crossing seam. This is associated to a significant decrease of the MECP energy, but also of the Spin Orbit (SO) coupling coefficient. Because the reaction is spin forbidden, the latter has a huge impact on the reaction rate, which is however counterbalanced by the large energy decrease. Remembering that, for unimolecular reactions, the characteristic reaction time is roughly equivalent to the inverse of the rate constant, the results reported in Table 5 show that the timescale for singlet-triplet interconversion in octacene and, quite likely, larger acenes, is abundantly below one millisecond at all temperatures, and about a hundred milliseconds or shorter above 1500 K in hexacene and heptacene. These timescales are comparable to the lifetime of PAHs containing a hundred or more atoms, as calculated through the kinetic simulations described below, thus indicating that PAHs triplet and singlet populations are likely to reach equilibrium during soot growth. This analysis of the reaction kinetics of even-C-numbered PAHs clearly indicates that their reactivity is best described as that of an open-shell singlet diradical or a triplet, rather than that of a closed-shell singlet.

Furthermore, by accounting for the open-shell character of large PAHs, it was possible to explain why large aromatic structures are often found to be alkylated [11, 45] despite the fact that H ipso-substitution reactions, exothermic by about 10 kcal/mol

and entropically favored, should rapidly lead to the loss of the alkyl group. Indeed, our calculations reveal that, following methyl addition and H loss, methylated acenes rapidly eject a hydrogen atom to form stable benzylic radicals. The radicals-to-molecules mole fraction ratio for methylated octacenes, calculated following the same procedure used for the considered odd-C-numbered PAHs in Fig. 1 and reported in Fig. 4, shows that methylated (and probably also otherwise alkylated) PAHs are more stable as radicals in typical soot growth conditions. As such, ipso-substitution reactions are not possible as they can take place only if the alkyl chain is not a radical center, since otherwise recombination would prevail.

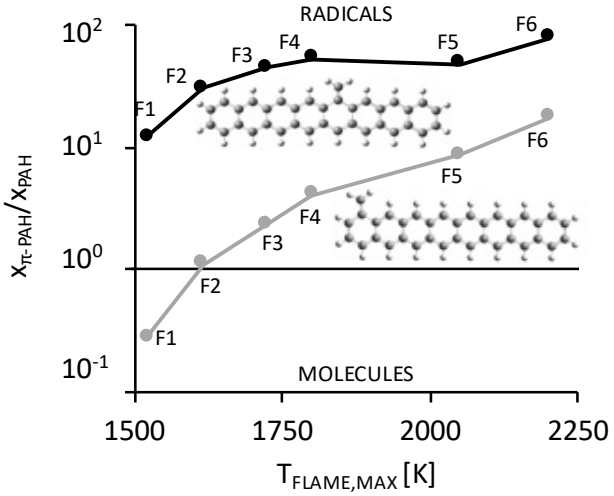

Fig. 4. Benzylic radicals-to-molecules mole fraction ratio calculated for 6 flames (see Fig. 1b) for octacene methylated in positions 2 and 8. Site numbering refers to Fig. 3.

3.3 Incorporating new radical-like chemistry in kinetic simulations

Coupling the results described in section 3.1 for even-C-numbered PAHs with those discussed for odd-C-numbered PAHs in section 3.2, we updated our soot kinetic model [9], accounting for the reactivity of particles and aggregates as that of radicals. The details of the model structure and numerical methods for kinetic simulations are reported in the section 2.4.

As it is often the case when building large PAH and soot mechanisms, rate constants for elementary and lumped reactions were determined through analogy with reactions whose kinetics is well established. The findings reported in the two previous sections indicate that the proper reference reactions to apply this methodology should use as PAH model a radical species. For this reason, rate constants of PAH

condensation onto particles and aggregates are determined through analogy with gas-phase reactions of π-radicals, like cyclopentadienyl and benzyl radicals (cC_5H_5, $C_6H_5CH_2$). The kinetics of HACA mechanism, i.e. one of the main soot growth pathways [6], is modified by neglecting particle surface activation though H-abstractions and adapting the kinetic constant of acetylene addition from analogy to the gas-phase reference reaction [31] C_2H_2 + $C_6H_5CH_2$. Likewise, soot surface oxidation by O_2 is described deriving the kinetics from reactions between O_2 and gas-phase π-radical PAHs [13, 32]. A comparison between the energy barriers computed for addition reactions of H, CH_3, $O(^3P)$, C_2H_2, and O_2 onto octacene and the activation energies adopted in the model for soot particles for the kinetics of gas-phase π-radical PAHs support this approach. For instance, the energy barriers of O_2+octacene discussed in Section 3.1, i.e. 5.5-24.9 kcal/mol, show very similar values compared to the activation energies of O_2+BIN5-25, i.e. 8-26.7 kcal/mol, adopted in the soot model. This corroborates the assumption of referring to the reactivity of stable radicals to describe that of soot particles in the discrete sectional soot model, in which even- and odd-C-numbered PAHs are not distinguished due to the extremely large size of the aromatic structures considered, with up to more the 300 million C-atoms, so as not to limit the use of the model even in the simplest 0-D, 1-D, and 2-D reactive flows simulations.

The updated kinetic model was used to simulate both soot formation in different flames (Fig. 5a) and soot oxidation (Fig. 5b and c). Soot oxidation was validated against a two-stage experimental setup [46] in which soot is firstly produced in high-temperature premixed flames and then oxidized in a plug flow reactor. The model accurately reproduces both the reduction of the peak of the measured particle size distributions and their shift towards smaller particles for increasing oxygen concentration. The model correctly accounts for the different reactivity of soot produced from different fuels, as the soot formed in an ethylene flame (Fig. 5b) is characterized by a lower oxidation rate than that formed in a toluene flame [47] (Fig. 5c). The model ability of accurately predicting soot oxidation has a significant relevance in corroborating the main assumption that soot species are persistent RSRs. Indeed, due to the absence of particle-surface activating species in the oxidative environment of the experimental setup, it was not possible to reproduce such experimental results via

state-of-the-art kinetic models based on established literature [13], mainly because they traditionally consider soot particles as almost inert closed-shell molecules. It was claimed [13] that neither increasing the oxidation rates, nor including particles oxidation by H_2O or catalysis of soot oxidation by water vapor decomposition, allowed soot depletion in such operative conditions.

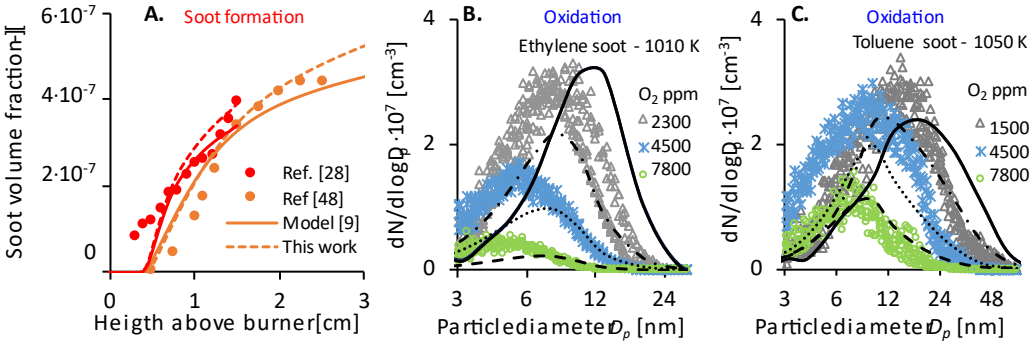

Fig. 5. Soot model validation. The soot model here proposed, which considers soot particles exclusively as stable radicals, is capable of predicting not only (a) the formation of soot in different laminar premixed flames [28, 48], but also (b and c) the oxidation of different types of soot at different temperatures [46]. N is the total particle number density. Symbols: experimental data; continuous lines: previous model [9] simulations; dashed lines: present model simulations (dash-dot 2300-1500 ppm; dot 4500 ppm; dashed 7800 ppm). In b and c all continuous lines overlap since oxidation is so slow in the previous model that it does not alter the initial particle size distribution.

Fig. 5 also shows the numerical simulations performed with the previous version of the model [9]. The predicted soot volume fractions in premixed flames [28, 48] are similar to those obtained with the updated model (Fig. 5a). Conversely, the previous model is not able to reproduce soot oxidation in the flow reactor [46] (Fig. 5b-c) and the corresponding particle size distributions remain unchanged with respect to the inlet conditions independently from temperature, O_2 concentration, and type of soot. The motivation for this behavior is the absence of abstracting species in the operating conditions of the considered reactor. Specifically, comparable soot inception and growth reaction rates are predicted by the two models in the two representative laminar premixed flames considered, as shown in Fig. 6. Indeed, in the updated model the persistent radical behavior of the soot pseudo species allows to neglect surface activation processes such as H-abstraction reactions enhancing particle reactivity, which is however partially counterbalanced by a lower rate of PAH condensation onto resonantly stabilized radical particles compared to that implemented in the previous

version of the model (see Section 2.4 and the detail soot kinetic model available as Supplementary Material). On the other hand, Fig. 6 clearly evidences that the oxidation rate predicted by the updated model is much faster than that of its previous version. This is of key relevance in order to describe the evolution of particle size distribution measured in [46]. Note that the very small oxidation rate reported in Fig. 6 is due to both the highly diluted conditions (dilution ratio ~100) and the very small concentration of O_2 (7800 ppm) fed to the flow reactor [46].

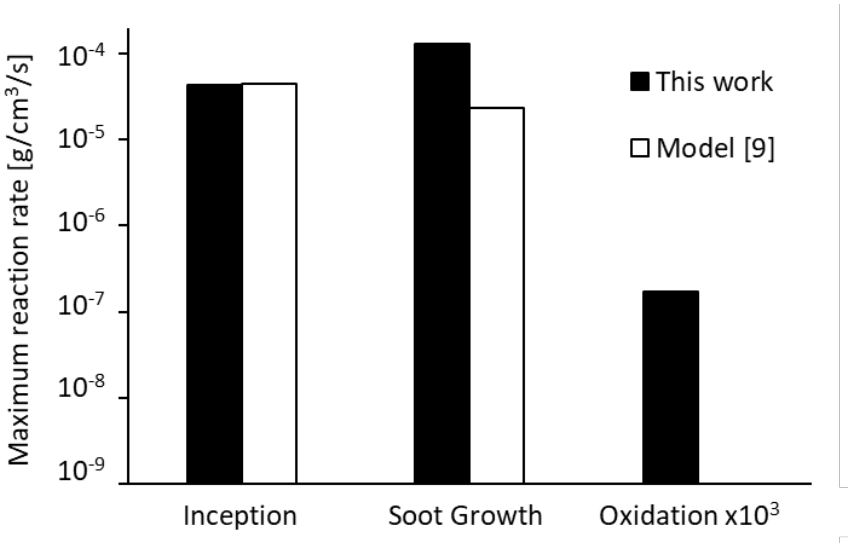

Fig. 6. Maximum reaction rates of soot inception and growth in premixed ethylene laminar flame [48] and of oxidation of ethylene soot by 7800 ppm of O_2 in the flow reactor [46].

4. Conclusions

The present theoretical and kinetic investigation of large PAHs reactivity led to the major conclusion that they exhibit radical behavior in combustion environments. PAHs with an odd number of carbon atoms preferentially form π-RSRs, while those with an even number of carbon atoms react as triplets. Based on these findings, we updated the existing CRECK soot model accounting for solid particles as persistent stable radicals. Model simulations not only satisfactorily reproduce soot formation, but also agree well with experimental soot oxidation data where existing kinetic mechanisms fail. A more extensive validation of the soot model will be performed in two upcoming papers, focused on the soot growth and oxidation mechanisms, respectively.

We believe the new concepts introduced in this work to be of key relevance in order to properly interpret the mechanisms of soot growth, oxidation, and inception.

Experimental validation will be needed to support the persistent radical behavior of large PAHs and carbonaceous particles theoretically predicted herein. For this purpose, acenes and their derivatives may serve as molecular models in order to investigate the reactivity of large PAHs, as it has been recently shown that it is possible to synthesize acenes with pronounced open shell character [49]. Accordingly, soot modeling activities and research efforts will have to consequently adapt to account for particles reactivity different from that considered in the kinetic models currently available in the literature. On the theoretical side, new computational tools may be required, as single reference electronic structure theories usually adopted to describe PAHs reactivity may fail to capture their open-shell character, in particular for H-abstraction reactions, and existing multi-reference theories are unsuitable to study large conjugated molecules such as PAHs. As the open-shell reactivity predicted for PAHs is independent of temperature, our deductions may have important implications on PAH reactivity in atmospheric environments and interstellar space, as well as on the study of materials with structures reminiscent of PAHs, such as graphene and carbon nanoparticles.

Finally, this work sheds light on a piece of evidence that has puzzled the kinetic community about large PAH structure for quite some time. Indeed, the presence of several aliphatic branches experimentally observed in large PAHs [11, 45] was explained through theoretical calculations on stable open-shell large acenes (e.g., octacene) representative of soot model molecules [6, 36-37]. Specifically, we evaluated the formation of stable alkylated acene radicals through methyl addition and H loss to be favored with respect to that of the molecular counterpart, where instead the entropically favored H ipso-substitution reactions should rapidly lead to the loss of the alkyl group.

Acknowledgments

This work is supported by MIUR with the PRIN 2017 2017PJ5XXX (MAGIC DUST) project.

References

[1] World Health Organization (WHO), Ambient air pollution: a global assessment of exposure and burden of disease (Publication 9789241511353, WHO, 2016; www.who.int/phe/publications/air-pollution-global-assessment/en/).

[2] J. Quaas, The soot factor, *Nature* 471 (2011) 456-457.

[3] Y. Yao, J. Pan, Z. Liu, X. Meng, W. Wang, H. Kan, W. Wang, Temporal association between particulate matter pollution and case fatality rate of COVID-19 in Wuhan, *Environ. Res.* 189 (2020) 109941.

[4] E. Bontempi, First data analysis about possible COVID-19 virus airborne diffusion due to air particulate matter (PM): the case of Lombardy (Italy), *Environ. Res*. 186 (2020) 109639.

[5] S. Li, Y. Ren, P. Biswas, S. D. Tse, Flame aerosol synthesis of nanostructured materials and functional devices: Processing, modeling, and diagnostics, *Prog. Energy Combust. Sci*. 55 (2016) 1-59.

[6] H. Wang, Formation of nascent soot and other condensed-phase materials in flames, *Proc. Combust. Inst*. 33 (2011) 41-67.

[7] K. O. Johansson, M. P. Head-Gordon, P. E. Schrader, K. R. Wilson, H. A. Michelsen, Resonance-stabilized hydrocarbon-radical chain reactions may explain soot inception and growth, *Science*. 361 (2018) 997–1000.

[8] A. Faccinetto, C. Irimiea, P. Minutolo, M. Commodo, A. D'Anna, N. Nuns, Y. Carpentier, C. Pirim, P. Desgroux, C. Focsa, X. Mercier, Evidence on the formation of dimers of polycyclic aromatic hydrocarbons in a laminar diffusion flame, *Commun. Chem*. 3 (2020) 1–8.

[9] W. Pejpichestakul, E. Ranzi, M. Pelucchi, A. Frassoldati, A. Cuoci, A. Parente, T. Faravelli, Examination of a soot model in premixed laminar flames at fuel-rich conditions, *Proc. Combust. Inst*. 37 (2019) 1013–1021.

[10] A. Keller, R. Kovacs, K. H. Homann, Large molecules, ions, radicals and small soot particles in fuel-rich hydrocarbon flames. Part IV. Large polycyclic aromatic hydrocarbons and their radicals in a fuel-rich benzene–oxygen flame, *Phys. Chem. Chem*. *Phys*. 2 (2000) 1667–1675.

[11] M. Commodo, K. Kaiser, G. De Falco, P. Minutolo, F. Schulz, A. D'Anna, L. Gross, On the early stages of soot formation: molecular structure elucidation by high-resolution atomic force microscopy, *Combust. Flame* 205 (2019) 154–164.

[12] M. Sirignano, J. Kent, A. D'Anna, Modeling Formation and Oxidation of Soot in Nonpremixed Flames, *Energy & Fuels* 27 (2013) 2303–2315.

[13] M. Frenklach, Z. Liu, R. I. Singh, G. R. Galimova, V. N. Azyazov, A. M. Mebel, Detailed, sterically-resolved modeling of soot oxidation: Role of O atoms, interplay with particle nanostructure, and emergence of inner particle burning, *Combust. Flame*. 188 (2018) 284–306.

[14] M. J. Frisch et al., Gaussian 09 (Gaussian, Inc., Wallingford, CT, USA, 2009).

[15] Y. Zhao, D. G. Truhlar, The M06 suite of density functionals for main group thermochemistry, thermochemical kinetics, noncovalent interactions, excited states, and transition elements: two new functionals and systematic testing of four M06-class functionals and 12 other function, *Theor. Chem. Acc.* 120 (2008) 215–241.
[16] M. J. Frisch, J. A. Pople, J. S. Binkley, Self-consistent molecular orbital methods 25. Supplementary functions for Gaussian basis sets, *J. Chem. Phys.* 80 (1984) 3265–3269.
[17] W. Siebrand, Radiationless Transitions in Polyatomic Molecules. II. Triplet-Ground-State Transitions in Aromatic Hydrocarbons, *J. Chem. Phys.* 47 (1967) 2411-2422.
[18] M. Mardirossian, M. Head-Gordon, How Accurate Are the Minnesota Density Functionals for Noncovalent Interactions, Isomerization Energies, Thermochemistry, and Barrier Heights Involving Molecules Composed of Main-Group Elements? *J. Chem. Theory Comput.* 12 (2016) 4303−4325.
[19] S. S. Zade, N. Zamoshchik, A. R. Reddy, G. Fridman-Marueli, D. Sheberla, M. Bendikov, Products and Mechanism of Acene Dimerization. A Computational Study, *J. Am. Chem. Soc.* 133 (2011) 10803–10816.
[20] Y. Georgievskii, J.A. Miller, M. P. Burke, S. J. Klippenstein, Reformulation and Solution of the Master Equation for Multiple-Well Chemical Reactions, *J. Phys. Chem. A.* 117 (2013) 12146–12154.
[21] C. Cavallotti, M. Pelucchi, Y. Georgievskii, S.J. Klippenstein, EStokTP: Electronic Structure to Temperature-and Pressure-Dependent Rate Constants-A Code for Automatically Predicting the Thermal Kinetics of Reactions, *J. Chem. Theory Comput.* 15 (2019) 1122-1145.
[22] T. Lu, F. Chen, Multiwfn: A Multifunctional Wavefunction Analyzer, *J. Comput. Chem.* 33 (2012) 580–592.
[23] A. D. Becke, A multicenter numerical integration scheme for polyatomic molecules, *J. Chem. Phys.* 88 (1988) 2547–2553.
[24] H. J. Werner, P. J. Knowles, G. Knizia, F. R. Manby, M. Schutz, “Molpro: a General-Purpose Quantum Chemistry Program Package”, 2012. http://www.molpro.net.
[25] A. Cuoci, A. Frassoldati, T. Faravelli, E. Ranzi, OpenSMOKE++: An object-oriented framework for the numerical modeling of reactive systems with detailed kinetic mechanisms, *Comput. Phys. Commun*. 192 (2015) 237-264.
[26] A. Ciajolo, A. D’Anna, R. Barbella, A. Tregrossi, A. Violi, The effect of temperature on soot inception in premixed ethylene flames, *Symp. Combust*. 26 (1996) 2327-2333.
[27] A.E. Bakali, J. L. Delfau, C. Vovelle, Experimental Study of 1 Atmosphere, Rich, Premixed n -heptane and iso-octane Flames, *Combust. Sci. Technol*. 140 (1998) 69–91.

[28] T. R. Melton, F. Inal, S.M. Senkan, The effects of equivalence ratio on the formation of polycyclic aromatic hydrocarbons and soot in premixed ethane flames, *Combust. Flame*. 121 (2000) 671–678.
[29] J. A. Cole, J. D. Bittner, J. P. Longwell, J. B. Howard, Formation mechanisms of aromatic compounds in aliphatic flames, *Combust. Flame* 56 (1984) 51–70.
[30] C. Saggese, A. Frassoldati, A. Cuoci, T. Faravelli, E. Ranzi, A wide range kinetic modeling study of pyrolysis and oxidation of benzene, *Combust. Flame* 160 (2013) 1168-1190.
[31] S. Fascella, C. Cavallotti, R. Rota, S. Carra, V. Mancinelli, The Peculiar Kinetics of the Reaction between Acetylene and the Cyclopentadienyl Radical, *J. Phys. Chem*. 109 (2005) 7546–7557.
[32] M. Pelucchi, C. Cavallotti, T. Faravelli, S. J. Klippenstein, H-Abstraction reactions by OH, HO2, O, O2 and benzyl radical addition to O2 and their implications for kinetic modelling of toluene oxidation, *Phys. Chem. Chem. Phys*. 20 (2018) 10607–10627.
[33] J. W. Martin, D. Hou, A. Menon, L. Pascazio, J. Akroyd, X. You, M. Kraft, Reactivity of Polycyclic Aromatic Hydrocarbon Soot Precursors: Implications of Localized Radicals on Rim-Based Pentagonal Rings, *J. Phys. Chem. C* 123 (2019) 26673–26682.
[34] B. S. Haynes, H. Gg. Wagner, Soot formation, *Prog. Energy Combust. Sci.* 7 (1981) 229-273.
[35] A. D'Anna, Combustion-formed nanoparticles, *Proc. Comb. Inst.* 32 (2009) 593–613.
[36] H.B. Zhang, X. You, C.K. Law, Role of Spin-Triplet Polycyclic Aromatic Hydrocarbons in Soot Surface Growth, *J. Phys. Chem. Lett.* 6 (2015) 477–481.
[37] H.B. Zhang, D. Hou, C.K. Law, X. You, Role of Carbon-Addition and Hydrogen-Migration Reactions in soot surface growth, *J. Phys. Chem. A* 120 (2016) 683-689.
[38] Y. Yang, E.R. Davidson, W. Yang, Nature of ground and electronic excited states of higher acenes, *Proc. Natl. Acad. Sci.* 113 (2016) E5098–E5107.
[39] J. Schiedt, R. Weinkauf, Photodetachment photoelectron spectroscopy of mass selected anions: anthracene and the anthracene-H_2O cluster, *Chem. Phys Lett.* 266 (1997) 201-205.
[40] J. Burgos, M. Pope, Ch. E. Swenberg, R.R. Alfano, Heterofission in pentacene-doped tetracene single crystals, *Phys. Stat. Sol. B* 83 (1977) 249-256.
[41] H. Angliker, E. Rommel, J. Wirz, Electronic spectra of hexacene in solution (ground state. Triplet state. Dication and dianion). *Chem. Phys Lett.* 87 (1982) 208–212.

[42] B. Hajgató, D. Szieberth, P. Geerlings, F. De Proft, M. S. Deleuze, A benchmark theoretical study of the electronic ground state and of the singlet-triplet split of benzene and linear acenes, *J. Chem. Phys.* 131 (2009) 224321.
[43] J. N. Harvey, Understanding the Kinetics of Spin-Forbidden Chemical Reactions. *Phys. Chem. Chem. Phys*. 9 (2007) 331−343.
[44] C. Cavallotti, C. De Falco, L. Pratali Maffei, A. Caracciolo, G. Vanuzzo, N. Balucani, P. Casavecchia, Theoretical Study of the Extent of Intersystem Crossing in the $O(^3P)+ C_6H_6$ Reaction with Experimental Validation *J. Phys. Chem. Lett.* 11 (2020) 9621−9628.
[45] B. D. Adamson, S. A. Skeen, M. Ahmed, N. Hansen, Detection of aliphatically bridged multi-core polycyclic aromatic hydrocarbons in sooting flames with atmospheric-sampling high-resolution tandem mass spectrometry, *J. Phys. Chem. A* 122 (2018) 9338-9349.
[46] J. Camacho, Y. Tao, H. Wang, Kinetics of nascent soot oxidation by molecular oxygen in a flow reactor, *Proc. Combust. Inst.* 35 (2015) 1887–1894.
[47] M. L. Botero, D. Chen, S. González-Calera, D. Jefferson, M. Kraft, HRTEM evaluation of soot particles produced by the non-premixed combustion of liquid fuels, *Carbon* 96 (2016) 459–473.
[48] F. Xu, P.B. Sunderland, G.M. Faeth, Soot formation in laminar premixed ethylene/air flames at atmospheric pressure, *Combust. Flame* 108 (1997) 471–493.
[49] Rudebusch, G. E. et al. Diindeno-fusion of an anthracene as a design strategy for stable organic biradicals. *Nat. Chem.* 8 (2016) 753–759.